NANOSYSTEMS:
PHYSICS, CHEMISTRY, MATHEMATICS

Ivanova A.A., et al. *Nanosystems: Phys. Chem. Math.*, 2026, **17** (1), 59–68.
http://nanojournal.ifmo.ru
DOI 10.17586/2220-8054-2026-17-1-59-68

Original article

The first example of synthesis Au-nanoparticles with amidine derivatives of *closo*-decaborate anion as stabilizing ligand

Arina A. Ivanova[1,2,a], Arina D. Filippova[2,b], Maria A. Teplonogova[2,c], Alexey A. Sadovnikov[2,3,d], Nikita A. Selivanov[2,e], Andrey P. Zhdanov[2,f], Konstantin Yu. Zhizhin[2,g], Nikolay T. Kuznetsov[2,h]

[1]Faculty of Chemistry, Higher School of Economics, Moscow, Russia
[2]Kurnakov Institute of General and Inorganic Chemistry of the Russian Academy of Sciences, Moscow, Russia
[3]Topchiev Institute of Petrochemical Synthesis, Russian Academy of Sciences, Moscow, Russia

[a]ivanova.arina112233@gmail.com, [b]arifilippova@yandex.ru, [c]m.teplonogova@gmail.com, [d]sadovnikov@ips.ac.ru, [e]goovee@yandex.ru, [f]zhdanov@igic.ras.ru, [g]zhizhin@igic.ras.ru, [h]boron@igic.ras.ru

Corresponding author: Andrey P. Zhdanov, zhdanov@igic.ras.ru

PACS 61.46.Df, 81.07.-b, 81.16.Be

ABSTRACT In this work, we report the one-pot aqueous synthesis of AuNPs using novel amidine derivatives of the *closo*-decaborate anion, functionalized with pendant thiol groups, as combined reducing and stabilizing agents. A comprehensive characterization using transmission electron microscopy (TEM) revealed the formation of nanoparticles with a distinctive and unusual hollow-core/dense-shell architecture, where a gold-rich shell encapsulates a low-Z element core. This unique morphology accounts for the observed absence of a characteristic surface plasmon resonance (SPR) band in the UV-Vis spectra, distinguishing these materials from classical solid-core AuNPs. X-ray photoelectron spectroscopy (XPS) confirmed the covalent attachment of the ligands via Au-S bonds and the integrity of the boron cage on the nanoparticle surface. The synthesis was optimized, establishing a 1:6 (Au:Ligand) molar ratio as ideal for achieving a narrow particle size distribution.

KEYWORDS boron cluster anion, closo-decaborate, amidine, cysteamine, gold nanoparticles

ACKNOWLEDGEMENTS This work was supported by Russian Science Foundation ((grant no. 24-13-00295, https://rscf.ru/project/24-13-00295/). This research was performed using the equipment of the JRC PMR IGIC RAS.

FOR CITATION Ivanova A.A., Filippova A.D., Teplonogova M.A., Sadovnikov A.A., Selivanov N.A., Zhdanov A.P., Zhizhin K.Yu., Kuznetsov N.T. The first example of synthesis Au-nanoparticles with amidine derivatives of *closo*-decaborate anion as stabilizing ligand. *Nanosystems: Phys. Chem. Math.*, 2026, **17** (1), 59–68.

1. Introduction

Gold nanoparticles (AuNPs) have garnered significant attention across diverse fields of modern research due to their unique physicochemical properties. Their biocompatibility, tunable optical characteristics, and ease of surface functionalization open vast possibilities for applications in medicine, biotechnology, and materials science. AuNPs are increasingly utilized for the detection and imaging of biomolecules, proteins, and nucleic acids at cellular and molecular levels [1], as well as for drug delivery [2] and as antioxidants [3].

The synthesis method critically determines the size, shape, and subsequently, the unique properties of the obtained nanomaterials [4, 5]. For instance, AuNPs smaller than 2 nm exhibit significant cytotoxicity due to nuclear penetration, whereas particles ranging from 15 to 30 nm are capable of permeating capillaries and tumor tissues [6]. Particle shape also dictates functionality; for example, gold nanospheres are preferred in diagnostics and drug delivery due to their structural consistency [7].

A particularly promising area of research involves the creation of conjugates between gold nanoparticles and boron clusters [8]. Boron cluster anions $[B_nH_n]^{2-}$ ($n = 10, 12$) possess essential properties such as high thermal stability, low toxicity, and a robust polyhedral framework, making them attractive for bio-applications, including biosensors and energy storage devices [9, 10]. A key application is Boron Neutron Capture Therapy (BNCT), a binary radiotherapeutic modality for treating locally aggressive tumors like gliomas and chordomas [11–14]. The efficacy of BNCT relies heavily on the selective accumulation of the non-radioactive boron-10 isotope in tumor cells. Consequently, the development of delivery agents that ensure high tumor-to-normal tissue ratios is of paramount importance.

Currently, the electrophile-induced nucleophilic substitution (EINS) of the $[B_{10}H_{10}]^{2-}$ anion is a well-established method for obtaining derivatives with a wide spectrum of functional groups [15, 16]. These derivatives can serve as stabilizing ligands for AuNPs, forming a monolayer with a specific chemical composition on the gold surface [17]. For example, recent studies reported AuNPs functionalized with polyethylene glycol thiols and inorganic cobalt bis(dicarbollide) derivatives, which showed high *in vivo* stability but limited tumor selectivity [18].

In this work, we report the synthesis of gold nanoparticles stabilized by novel amidine derivatives of the *closo*-decaborate anion containing pendant thiol groups. We investigate the synthesis of the ligand systems via nucleophilic addition of cysteamine to nitrilium derivatives of $[B_{10}H_{10}]^{2-}$ and explore the formation of AuNPs. A notable feature of the obtained nanoparticles is the absence of a characteristic surface plasmon resonance (SPR) band, which distinguishes them from classical citrate- or thiol-stabilized gold colloids. The structural features, morphology, and chemical composition of the hybrid nanomaterials are discussed in detail.

2. Experimental

2.1. Methods

2.1.1. IR spectra were recorded on an FT-08 Infralum infrared spectrometer in the range of 4000 – 600 cm^{-1} with a resolution of 1 cm^{-1}. Samples were prepared as KBr pellets.

2.1.2. ^{1}H, $^{13}C\{^{1}H\}$, $^{11}B\{^{1}H\}$ *NMR spectra* of solutions in CD_3CN were recorded on a q-ONE AS400 Quantum I Plus spectrometer at frequencies of 399.879, 161.874, 128.297 MHz, respectively, with internal deuterium stabilization. TMS and $BF_3{\cdot}OEt_2$ were used as external standards, respectively.

2.1.3. High-resolution mass spectra were recorded on a LCMS-9030 device (Shimadzu, Japan) by electrospray ionization mass spectrometry (ESI-MS). Measurements were carried out in negative and positive ion mode; samples were dissolved in acetonitrile and injected into the mass-spectrometer chamber from an HPLC system LC-40 Nexera (Shimadzu, Japan). The following parameters were used: capillary voltage -3.0 kV (4 kV for positive ions); mass scanning range: m/z 50 – 1000; external calibration with solution NaI in MeOH/H_2O; drying and heating gases (nitrogen) (each 10 L/min); nebulizing gas (nitrogen) (3 L/min); interface temperature: 250 °C; flow rate 100 % acetonitrile or (50:50 (v/v) acetonitrile/water 0.4 mL/min. Molecular ions in the spectra were analyzed and matched with the appropriately calculated *m/z* and isotopic profiles in the LabSolutions v.5.114 program.

2.1.4. Dynamic light scattering (DLS) and ζ-potential measurements were carried out at 20 °C, using a Photocor Compact-Z analyser (Photocor, Moscow, Russia) equipped with a 636.65 nm laser. The correlation function for each sample was obtained by averaging ten curves, each being acquired for 20 s. The hydrodynamic diameter of aggregates was determined using DynalS software (Moscow, Russia).

2.1.5. Scanning electron microscopy (SEM) and scanning transmission electron microscopy (STEM) images were taken using a Tescan Amber GMH scanning electron microscope. STEM images were acquired using a R-STEM detector at magnifications of × 200,000 – 900,000 with an accelerating voltage of 30 kV. To obtained STEM images, sols were dropped on a copper grid coated with formvar and dried at room temperature overnight. SEM images were obtained using an Everhart–Thornley detector at an accelerating voltage of 1 kV. To obtain SEM images, sols were dropped on the carbon tape and dried at room temperature overnight.

2.1.6. The XPS measurements were performed using a "PREVAC EA15" electron spectrometer. In the current work, AlKα ($h\nu = 1486.6$ eV, 150 W) were used as a primary radiation source. The pressure in analytical chamber did not exceed $5 \cdot 10^{-9}$ mbar during spectra acquisition. The binding energy (BE) scale was pre-calibrated using the positions of Ag3d5/2 (368.3 eV) from silver foils. Samples in the form of a suspension of colloidal particles after dialysis were supported to the holder. To take into account the effect of surface charging, the C1s at ($Eb = 284.8$ eV) from the carbon was used as an internal standard.

2.2. Synthetic protocols

2-Aminoethanethiol (ABCR, 98 %), $H[AuCl_4]{\cdot}(H_2O)_n$ (Acros Organic), $Na[BPh_4]$ (ABCR, 98 %) were used without additional purification. All solvents were purified according to the literature method [19]. Nitrilium derivatives of *closo*-decaborate anion $(Bu_4N)[2\text{-}B_{10}H_9NCR]$ ($R = Et$ [20], ^{n}Pr [20], ^{i}Pr [20]) were synthesized by known procedures.

2.2.1. General procedure for the synthesis of amidine derivatives (Bu_4N*)[2-*$B_{10}H_9NH{=}C(NHC_2H_4SH)R$*] (*$R = Et$ *(4),* ^{n}Pr *(5),* ^{i}Pr *(6)).* A mixture of the corresponding nitrilium derivative 1–3 (1.0 mmol) and cysteamine (304 mg, 2.0 mmol) was dissolved in methanol (10 mL). The reaction mixture was stirred under a dry argon atmosphere for 30 min and then concentrated on a rotary evaporator. The residue was dissolved in CH_2Cl_2 (5 mL) and washed successively with aqueous hydrazine hydrate solution and distilled water until neutral pH. The organic phase was dried over anhydrous Na_2SO_4, filtered, and concentrated to dryness.

2.2.2. (Bu$_4$N)[2-B$_{10}$H$_9$NH=C(Et)NHC$_2$H$_4$SH] (4). IR (KBr, cm^{-1}): 3425, 3296, 3233 ν (N–H), 2475 ν (B–H), 1636 ν (C=N). ^{11}B{^{1}H}-NMR (CD$_3$CN) δ (ppm): 1.6 (s, 1B, B(10)), -5.9 (s, 1B, B(1)), -16.5 (s, 1B, B(2)), -25.2 (s, 4B, B(3,5,6,7)), -28.2 (s, 3B, B(4,8,9)). ^{1}H NMR (CD$_3$CN) δ (ppm): 8.43 (br.s., 1H, N**H**–C), 6.37 (br.s., 1H, N**H**=C), 3.68 (m, 2H, N–C**H**$_2$CH$_2$SH), 3.31 (8H, Bu$_4$N), 3.00 (t, 2H, N–CH$_2$C**H**$_2$SH, 7 Hz), 2.41 (q, 2H, C**H**$_2$CH$_3$, 8 Hz), 1.70 (8H, Bu$_4$N), 1.33 (8H, Bu$_4$N), 1.01 (t, 3H, CH$_2$C**H**$_3$, 8 Hz), 0.87 (12H, Bu$_4$N). ^{13}C NMR (CD$_3$CN) δ (ppm): 169.8 (NH=**C**–CH$_2$CH$_3$), 58.6 (Bu$_4$N), 41.8 (N**C**H$_2$CH$_2$SH), 37.5 (NCH$_2$**C**H$_2$SH), 24.9 (NH=C–**C**H$_2$CH$_3$), 23.9 (Bu$_4$N), 19.7 (Bu$_4$N), 13.2 (Bu$_4$N), 10.3 (NH=C-CH$_2$**C**H$_3$). HRMS(ESI) m/z: 248.2336 (found for [(B$_{10}$H$_9$NHC(C$_2$H$_5$)NH$_2$C$_2$H$_4$S)$_2$]$^{2-}$, calculated for [A]$^{2-}$ 248.2351).

2.2.3. (Bu$_4$N)[2-B$_{10}$H$_9$NH=C(^{n}Pr)NHC$_2$H$_4$SH] (5). IR (KBr, cm^{-1}): 3415, 3296, 3233 ν (N–H), 2478 ν (B–H), 1632 ν (C=N). ^{11}B{^{1}H} NMR (CD$_3$CN) δ (ppm): 1.1 (s, 1B, B(10)), -6.1 (s, 1B, B(1)), -17.0 (s, 1B, B(2)), -25.7 (s, 4B, B(3,5,6,7)), -28.7 (s, 3B, B(4,8,9)). ^{1}H NMR (CD$_3$CN) δ (ppm): 8.43 (br.s., 1H, N**H**–C), 6.13 (br.s., 1H, N**H**=C), 3.67 (m, 2H, N–C**H**$_2$CH$_2$SH), 3.08 + 3.01 (m, 10H, Bu$_4$N + N–CH$_2$C**H**$_2$SH), 2.28 (q, 2H, C**H**$_2$CH$_2$CH$_3$, 8 Hz), 1.59 (8H, Bu$_4$N), 1.48 (m, 2H, CH$_2$C**H**$_2$CH$_3$), 1.36 (8H, Bu$_4$N), 0.96 (12H, Bu$_4$N), 0.89 (t, 3H, CH$_2$CH$_2$C**H**$_3$, 8 Hz). ^{13}C NMR (CD$_3$CN) δ (ppm): 167.8 (NH=**C**–CH$_3$), 59.2 (Bu$_4$N), 42.6 (N**C**H$_2$CH$_2$SH), 40.1 (NCH$_2$**C**H$_2$SH), 25.5 (NH=C–**C**H$_2$CH$_2$CH$_3$), 24.2 (Bu$_4$N), 20.7 (NH=C–CH$_2$**C**H$_2$CH$_3$), 20.1 (Bu$_4$N), 13.7 (Bu$_4$N), 13.5 (NH=C-CH$_2$CH$_2$**C**H$_3$). HRMS(ESI) *m/z*: 262.2523 (found for [(B$_{10}$H$_9$NHC(C$_3$H$_7$)NH$_2$C$_2$H$_4$S)$_2$]$^{2-}$, calculated for [A]$^{2-}$ 262.2507); 264.2546 (found for [B$_{10}$H$_9$NHC(C$_3$H$_7$)NH$_2$C$_2$H$_4$SH]$^{1-}$, calculated for [A]$^{1-}$ 264.2549).

2.2.4. (Bu$_4$N)[2-B$_{10}$H$_9$NH=C(^{i}Pr)NHC$_2$H$_4$SH] (6). IR (KBr, cm^{-1}): 3420, 3292, 3235 ν (N–H), 2501 ν (B–H), 1640 ν (C=N). ^{11}B{^{1}H} NMR (CD$_3$CN) δ (ppm): 1.1 (s, 1B, B(10)), -6.1 (s, 1B, B(1)), -16.4 (s, 1B, B(2)), -25.5 (s, 4B, B(3,5,6,7)),-28.6 (s, 3B, B(4,8,9)). ^{1}H NMR (CD$_3$CN) δ (ppm): 8.48 (br.s., 1H, N**H**–C), 5.72 (br.s., 1H, N**H**=C), 3.74 (m, 2H, N–C**H**$_2$CH$_2$SH), 3.09 + 3.03 (m, 10H, Bu$_4$N + N–CH$_2$C**H**$_2$SH), 2.89 (m, 1H, C**H**(CH$_3$)$_2$), 1.60 (8H, Bu$_4$N), 1.35 (8H, Bu$_4$N), 1.04 (d, 6H, CH(**C**H$_3$)$_2$,7 Hz), 0.96 (12H, Bu$_4$N). ^{13}C NMR (CD$_3$CN) δ (ppm): 173.0 (NH=**C**–CH$_3$), 59.2 (Bu$_4$N), 42.0 (N**C**H$_2$CH$_2$SH), 38.4 (NCH$_2$**C**H$_2$SH), 29.2 (NH=C–**C**H(CH$_3$)$_2$), 24,2 (Bu$_4$N), 20.2 (Bu$_4$N), 19.2 (NH=C–CH(**C**H$_3$)$_2$), 13.8 (Bu$_4$N). HRMS(ESI) *m/z*: 262.2520 (found for [(B$_{10}$H$_9$NHC(C$_3$H$_7$)NH$_2$C$_2$H$_4$S)$_2$]$^{2-}$, calculated for [A]$^{2-}$ 262.2507).

2.2.5. Preparation of sodium salts. The corresponding tetrabutylammonium salt 4–6 (0.5 mmol) was dissolved in ethanol (10 mL) and treated with an aqueous solution of sodium tetraphenylborate (155 mg, 0.45 mmol) under stirring for 30 min. The formation of a fine white precipitate (Bu$_4$N)[BPh$_4$] was observed. The mixture was filtered, and the filtrate was concentrated on a rotary evaporator. The residue was recrystallized from an acetonitrile / diethyl ether mixture to yield the sodium salts Na[2-B$_{10}$H$_9$NH=C(NHC$_2$H$_4$SH)R].

2.2.6. Synthesis of gold nanoparticles (AuNPs). Gold nanoparticles were synthesized via the direct reaction of hydrogen tetrachloroaurate H[AuCl$_4$] with the sodium salts of the amidine-functionalized *closo*-decaborates. In a typical procedure, an aqueous solution of H[AuCl$_4$] (0.025 M) was mixed with an aqueous solution of the ligand **Na(4–6)** at molar ratios ranging from 1:1 to 1:12 (Au:Ligand). The mixture was stirred for 30 min at room temperature, during which the solution turned a reddish-brown color. The resulting sol was centrifuged to remove bulk by-products (borates), and the supernatant was filtered through a 200 nm PTFE filter.

3. Results and discussions

3.1. Synthesis and characterization of amidine ligands

Novel amidine derivatives of the *closo*-decaborate anion were synthesized via the nucleophilic addition of cysteamine to the triple bond of nitrilium derivatives [2-B$_{10}$H$_9$NCR]$^{1-}$ (R=Et, ^{n}Pr, ^{i}Pr) in methanol (Fig. 1). The reaction progress was monitored by ^{11}B NMR spectroscopy (Fig. 4). The formation of the amidine functionality is evidenced by characteristic changes in the chemical shifts of the boron cage atoms. Specifically, the signal of the substituted boron atom B(2) shifts downfield to the range of -15.5 to -17.0 ppm compared to the initial nitrilium derivative. Concurrently, the signal of the antipodal apical atom B(10) appears in the region of 1.0 – 1.6 ppm, while the signal of the proximal apical atom B(1) undergoes a significant upfield shift to the range of -4.8 to -6.3 ppm (Fig. 2).

The structure of the obtained compounds was further confirmed by ^{1}H and ^{13}C NMR spectroscopy and high-resolution ESI-MS. For instance, the ^{1}H NMR spectrum of compound **5** (Fig. 3a) displays distinct signals corresponding to the iso-propyl group of the amidine fragment and the ethylene linker of the cysteamine moiety. The ESI-HRMS data are in good agreement with the calculated isotopic profiles for the dianionic species [(B$_{10}$H$_9$NHC(R)NH$_2$C$_2$H$_4$S)$_2$]$^{2-}$ (disulfide form) and monoanionic species (thiol form), confirming the integrity of the boron cage and the ligand attachment. To facilitate water solubility for subsequent AuNP synthesis, the derivatives were converted into their sodium salts via metathesis with sodium tetraphenylborate.

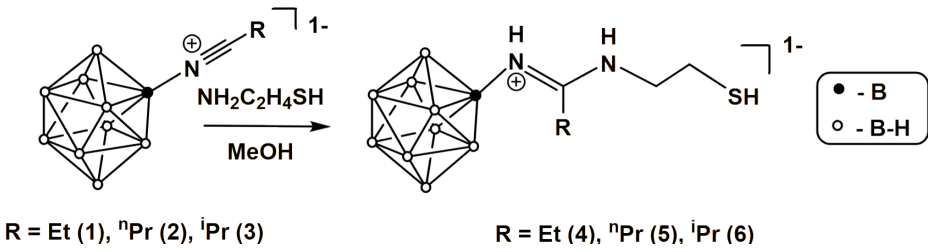

FIG. 1. General scheme of synthesis of *closo*-borate amidine **4-6**

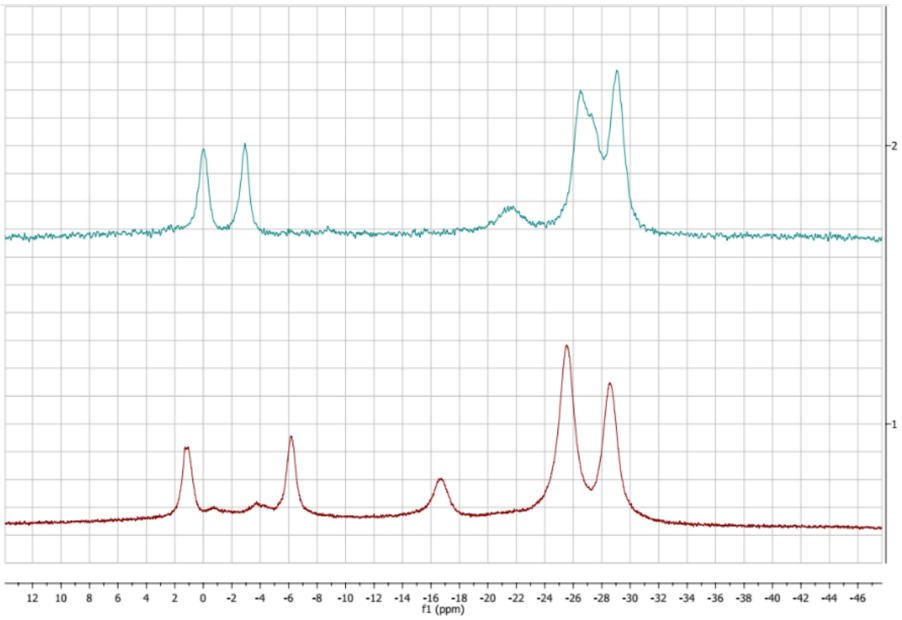

FIG. 2. $^{11}B\{^1H\}$ NMR spectra of $(Bu_4N)[2\text{-}B_{10}H_9NCC_2H_5]$ (1) (top) and $(Bu_4N)[2\text{-}B_{10}H_9(NHC(C_2H_5)NHC_2H_4SH]$ (4) (bottom)

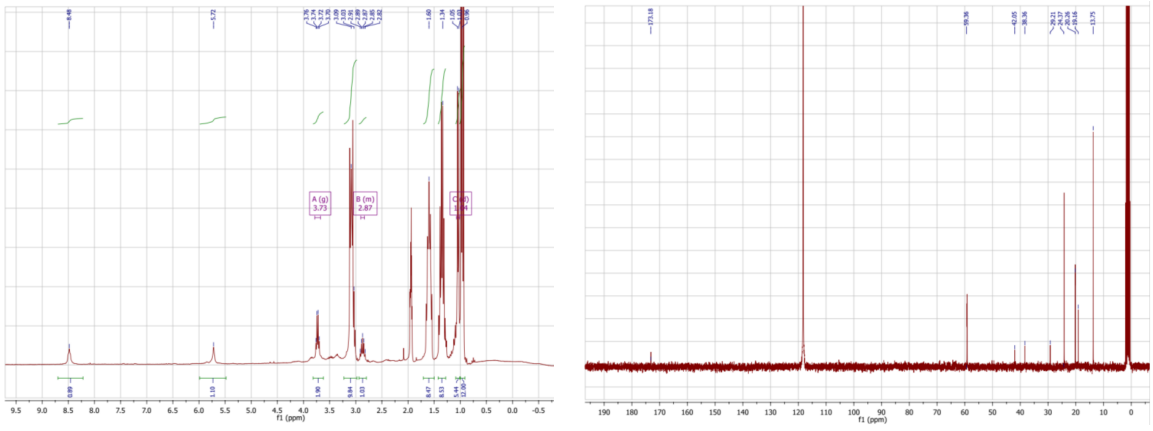

(a) (b)

FIG. 3. ^1H NMR (a) and ^{13}C NMR (b) spectra of $(Bu_4N)[2\text{-}B_{10}H_9(NHC(^iC_3H_7)NHC_2H_4SH]$ (6)

3.2. Synthesis and morphology of gold nanoparticles

Gold nanoparticles were synthesized by the direct reduction/stabilization method using sodium salts of the synthesized ligands **Na(4–6)** and $H[AuCl_4]$ in aqueous solution. This approach aimed to produce biocompatible AuNPs with a core size suitable for medical applications (¡ 100 nm). In this process, the boron cluster derivative acts as a stabilizing agent through the formation of strong Au–S bonds via the pendant thiol group.

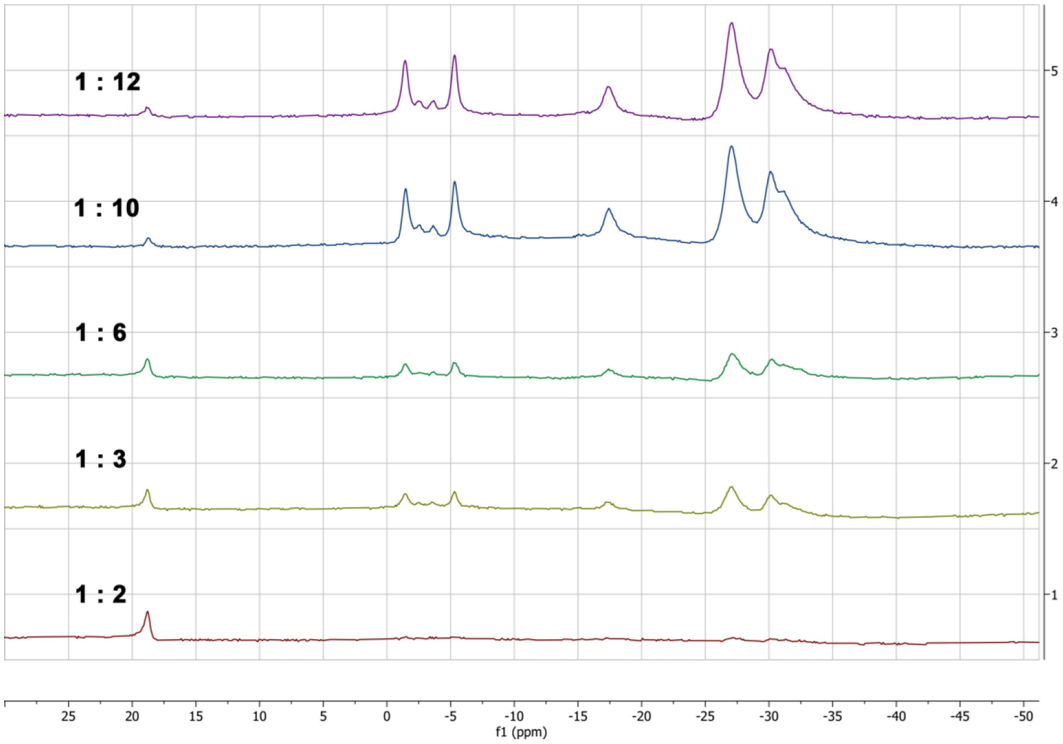

FIG. 4. $^{11}B\{^1H\}$ NMR of AuNPs@Na(6) sols obtained by varying the molar ratio Au^{3+} : Na(6).

The reagent ratio (Au^{3+} : Ligand) was optimized by varying the molar ratio from 1:1 to 1:12. The optimization was guided by DLS measurements and $^{11}B\{^1H\}$ NMR spectroscopy of the reaction supernatants. At low ligand ratios (1:1 and 1:2), $^{11}B\{^1H\}$ NMR spectra revealed the disappearance of the cluster signals and the emergence of a signal at 19 – 20 ppm characteristic of borates ($B(OH)_3$), indicating the oxidative degradation of the boron cage by Au(III) species. Conversely, at ratios of 1:6 and higher, the integrity of the excess ligand was preserved (Fig. 4).

DLS analysis (Fig. 5) indicated that the optimal hydrodynamic size and polydispersity were achieved at a ratio of 1:6. For example, AuNPs stabilized by ligand **Na(6)** exhibited a hydrodynamic diameter of approximately 51 nm. Increasing the ligand excess further (1:10, 1:12) led to a slight increase in the mean diameter but maintained a narrow size distribution. It also leads to excessive consumption of the cluster ligand.

The morphology of the obtained nanoparticles was investigated by SEM and STEM (Figs. 6, 7). The sample AuNPs@Na(6) consists of aggregated spherical nanoparticles with a diameter of approximately 20 – 30 nm. The sample AuNPs@Na(5) formed larger spheres (40 – 80 nm). STEM images reveal a core-shell structure where the dense gold shell is surrounded by a lighter organic contrast, attributed to the boron-cluster ligand shell. It is important to note that the ring-like structures observed in some micrographs are actually spheres observed in a transmission (STEM) mode, as confirmed by SEM images showing solid spherical particles (Fig. 7).

Specifically, the particles appear to consist of a low-Z element core (likely composed of boron cluster aggregates or solvent-swollen organic phase) surrounded by a dense gold shell. This gold shell is, in turn, stabilized by an outer layer of the amidine-boron ligands. Such a multi-layered structure (“organic core”@“Au shell”@“ligand corona”) is distinct from classical solid gold nanoparticles. This unique morphology may also explain the absence of the typical surface plasmon resonance band in the UV-Vis spectra, as the optical response of gold nanoshells is highly sensitive to the shell thickness and core dielectric constant, often shifting the plasmon band into the near-infrared region or broadening it significantly. The formation of agglomerates inside the particles may be associated with the tendency of salts of the $[B_{10}H_{10}]^{2-}$ anion to form coordination compounds with gold with the formation of M–B bonds [21].

Having established the optimal reagent ratio (1:6), we compared the hydrodynamic size distributions of AuNPs stabilized by ligands **Na(4)**, **Na(5)**, and **Na(6)**. As shown in Fig. 7, all three ligands facilitate the formation of relatively monodisperse nanoparticles. However, the nature of the alkyl substituent in the amidine fragment influences the final particle size. AuNPs stabilized by the ethyl-substituted ligand **Na(4)** and *n*-propyl-substituted **Na(5)** exhibit slightly

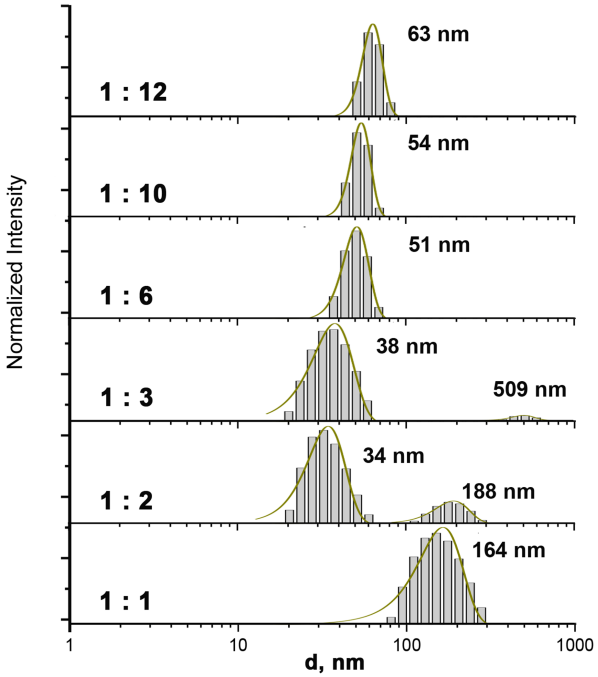

FIG. 5. DLS analysis of AuNPs@Na(6) sols obtained by varying the molar ratio Au^{3+} : Na(6)

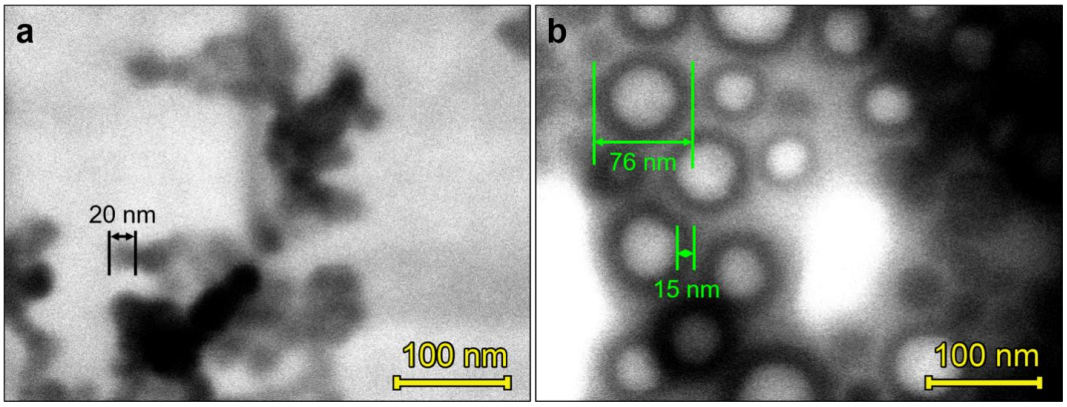

FIG. 6. STEM images of a) AuNPs@Na(6) and b) AuNPs@Na5 samples taken in a bright field mode

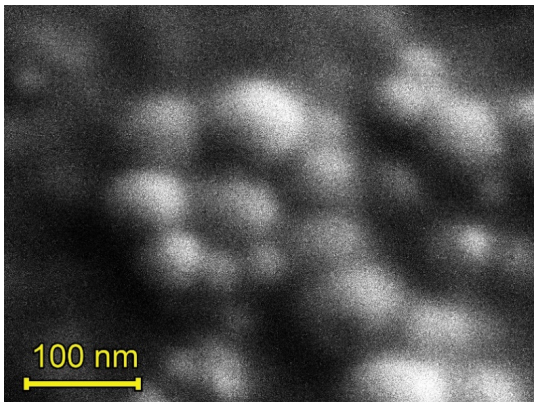

FIG. 7. SEM image of AuNPs@Na5 sample

larger hydrodynamic diameters compared to the *i*-propyl derivative **Na(6)**. This trend suggests that the steric hindrance of the branched isopropyl group in **Na(6)** may provide more effective surface screening during the nucleation and growth stages, limiting the final aggregate size more efficiently than the linear alkyl chains.

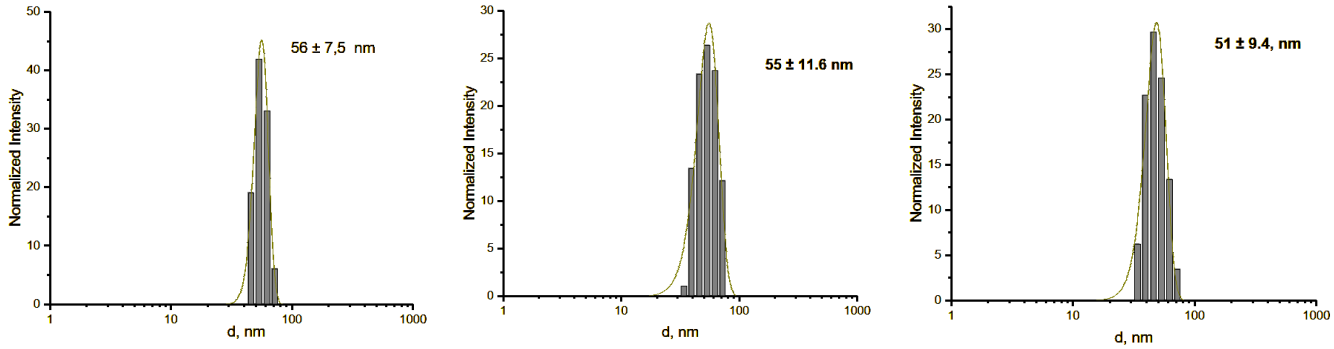

(a) (b) (c)

FIG. 8. DLS analysis of AuNPs@Na(4) (a), AuNPs@Na(5) (b) and AuNPs@Na(6) (c) sols obtained by the molar ratio Au^{3+} : Ligand 1 : 6

3.3. Surface chemistry (XPS Analysis)

X-ray photoelectron spectroscopy (XPS) confirmed the elemental composition of the nanoparticles (Au, S, B, N, C, O) (Figs. 8–10). The Au4f7/2 binding energy in Na(4)–Na(6) samples is ∼84.5 eV. The value of the binding energy is higher than that of the gold foil (84.0 eV), which is due to the influence of the particle size [22,23]. The B1s signals show the presence of two major components: B–B bonds in the cluster with binding energies at ∼187.5 eV, and a small amount of boron (III) in B_2O_3 or $B(OH)_3$ up to 15 % at ∼192.0 eV, respectively [24, 25]. The S2p signals show the presence of two major components: Au–S bonds with binding energies at 162.7-162.8 eV (S2p3/2) and at ∼163.9 eV (S2p1/2), and just 40 – 60 % of unbound thiol characterized by two components in a 2:1 ratio at ∼163.8 eV (S2p3/2) and 164.9 eV (S2p1/2), respectively [22, 23].

3.4. Stability and purification

Initially, the crude colloidal solutions exhibited a tendency toward gradual agglomeration upon concentration, likely due to the high ionic strength arising from the excess reagents and by-products (sodium salts, borates). However, we found that purification of the sols via dialysis against distilled water significantly enhanced their colloidal stability. The dialyzed sols of Na(4)–Na(6) stabilized AuNPs retained their optical properties and hydrodynamic size distribution for several months when stored at 4 °C. This enhanced stability confirms that the *closo*-decaborate amidine derivatives form a robust stabilizing shell, and the removal of destabilizing electrolytes is the key step for obtaining long-term stable dispersions suitable for biological studies.

4. Conclusions

In summary, we have successfully developed a synthetic route for novel amidine derivatives of the *closo*-decaborate anion functionalized with pendant thiol groups. These compounds were used for the first time as combined reducing and stabilizing agents for the one-pot synthesis of gold nanoparticles in an aqueous medium.

A key finding of this work is the formation of nanoparticles with an unconventional low-density core/dense-shell architecture, where a gold-rich shell encapsulates a core composed of low-Z elements, likely boron cluster aggregates. This unique morphology is responsible for the observed absence of a characteristic surface plasmon resonance band, distinguishing these materials from classical solid-core AuNPs.

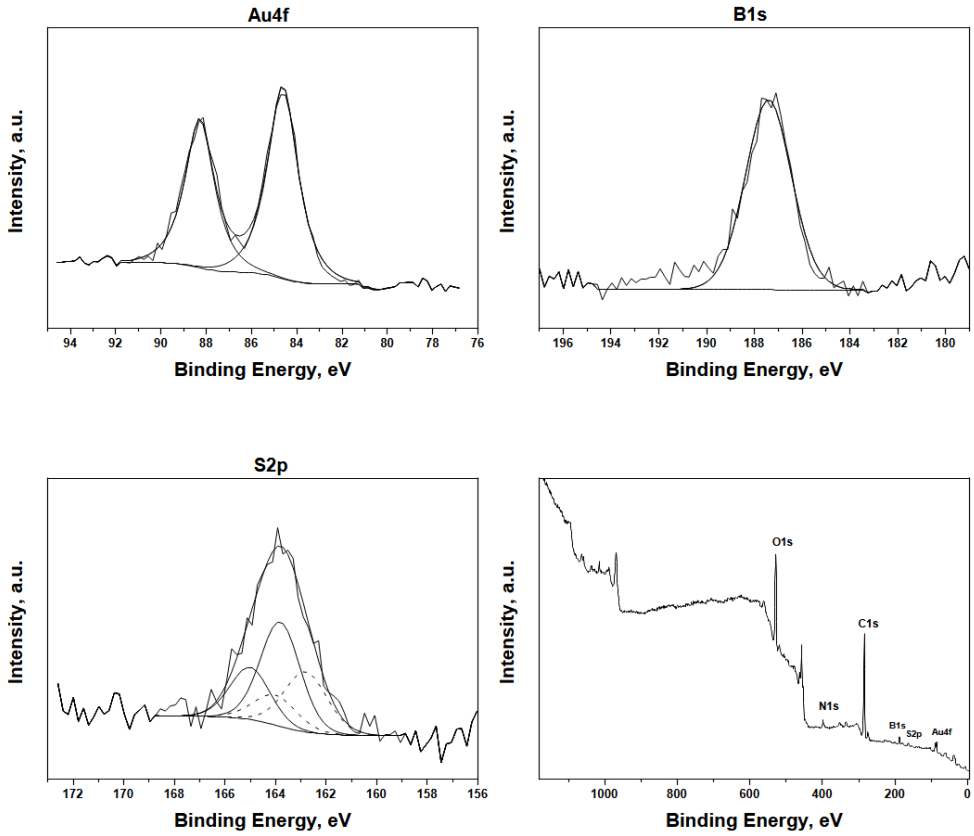

FIG. 9. XPS Au4f, B1s, S2p and survey spectra of AuNPs@Na(4)

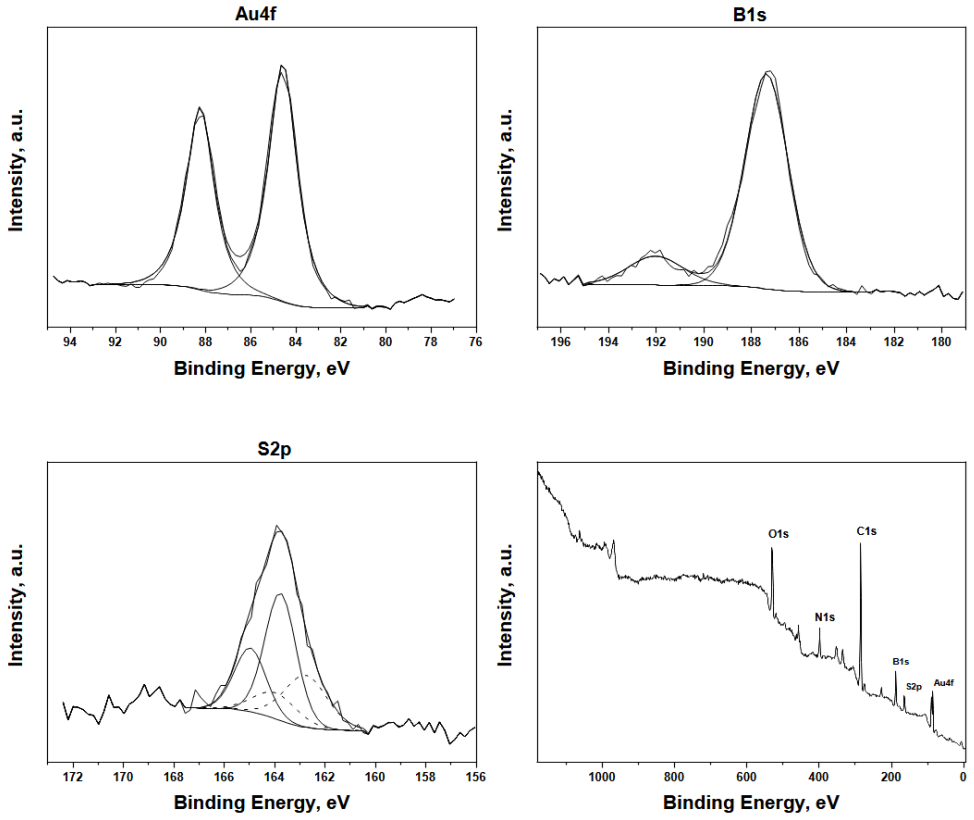

FIG. 10. XPS Au4f, B1s, S2p and survey spectra of AuNPs@Na(5).

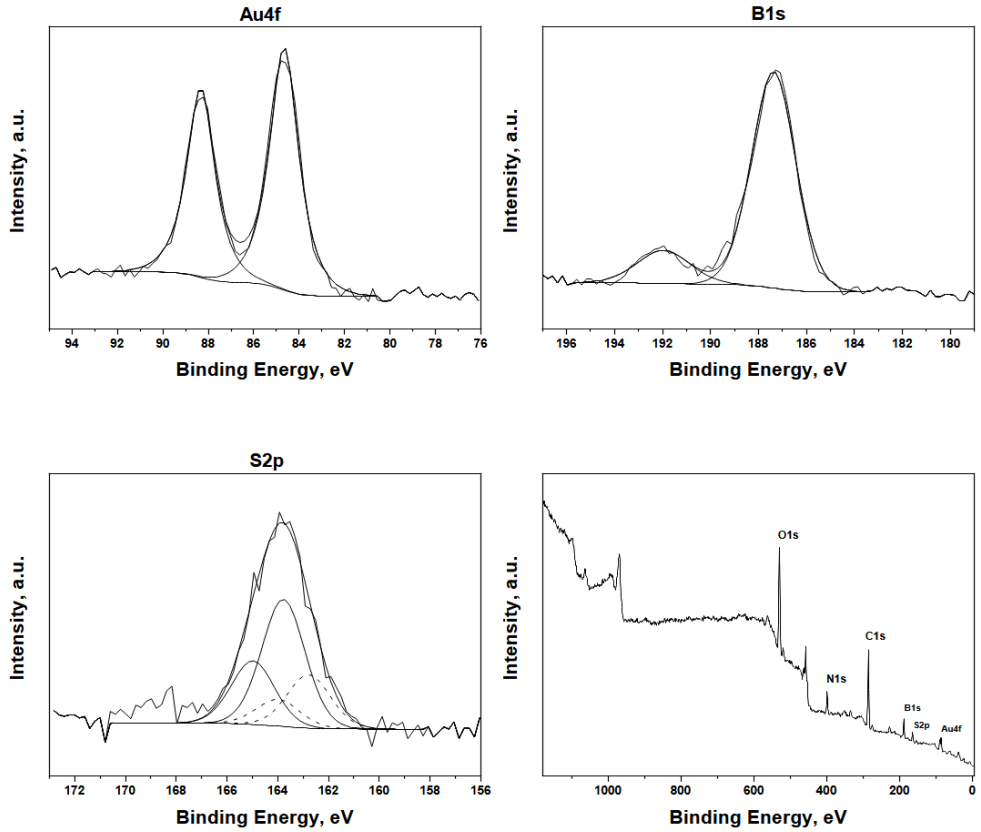

FIG. 11. XPS Au4f, B1s, S2p and survey spectra of AuNPs@Na(6)

References

[1] Fernandes D.A. Multifunctional gold nanoparticles for cancer theranostics. *3 Biotech*, 2024, **14**, 267.

[2] Tan D.K., Tai Y., Nguyen T.T. Gold nanoparticles for targeting of biomedical applications: A review. *Asian J. Chem.*, 2024, **36** (8), P. 1741–1746.

[3] Asih S., Budi S., Katas H. Synthesis and application of gold nanoparticles as antioxidants. *Pharmacia*, 2024, **71**, P. 1–19.

[4] Kattumuri V., Katti K., Bhaskaran S., et al. Gum arabic as a phytochemical construct for the stabilization of gold nanoparticles: in vivo pharmacokinetics and X-ray-contrast-imaging studies. *Small*, 2007, **3** (2), P. 333–341.

[5] Nirmala J.G., Rachineni K., Choudhary S., et al. Triphala polyphenols-functionalized gold nanoparticles impair cancer cell survival through induction of tubulin dysfunction. *J. Drug Deliv. Sci. Technol.*, 2021, **61**, 102167.

[6] Xia Y., Wu X., Zhao J., et al. Three dimensional plasmonic assemblies of AuNPs with an overall size of sub-200 nm for chemo-photothermal synergistic therapy of breast cancer. *Nanoscale*, 2016, **8** (44), P. 18682–18692.

[7] Zhao R., Xiang J., Wang B., et al. Recent advances in the development of noble metal NPs for cancer therapy. *Bioinorg. Chem. Appl.*, 2022, **2022**, 2444516.

[8] Sakore P., Gaikwad S., Aadil K.R., et al. The theranostic potential of green nanotechnology-enabled gold nanoparticles in cancer: A paradigm shift on diagnosis and treatment approaches. *Results Chem.*, 2024, **7**, 101264.

[9] Amendola V., Pilot R., Frasconi M., et al. Surface plasmon resonance in gold nanoparticles: a review. *J. Phys.: Condens. Matter*, 2017, **29** (20), 203002.

[10] Huang X., El-Sayed M.A. Gold nanoparticles: Optical properties and implementations in cancer diagnosis and photothermal therapy. *J. Adv. Res.*, 2010, **1** (1), P. 13–28.

[11] Wu C.-Y., Hsieh H.-H., Chang T.-Y., et al. Development of MRI-detectable boron-containing gold nanoparticle-encapsulated biodegradable polymeric matrix for boron neutron capture therapy (BNCT). *Int. J. Mol. Sci.*, 2021, **22**, 8050.

[12] Ready A.D., Nelson Y.A., Torres Pomares D.F., Spokoyny A.M. Redox-active boron clusters. *Acc. Chem. Res.*, 2024, **57**, P. 1310–1324.

[13] Ohta K. Basic organic and inorganic chemistry of boron clusters and its application to drug discovery. *Yakugaku Zasshi*, 2022, **142** (8), P. 855–863.

[14] Soriano-Ursúa M.A. Boron applications in prevention, diagnosis and therapy for high global burden diseases. *Inorganics*, 2023, **11** (9), 358.

[15] Hirose K., Konishi T., Tanaka H., et al. Boron neutron capture therapy using cyclotron-based epithermal neutron source and borofalan (^{10}B) for recurrent or locally advanced head and neck cancer (JHN002): An open-label phase II trial. *Radiother. Oncol.*, 2021, **155**, P. 182–187.

[16] Fujikawa Y., Kawabata S., Tsujino K. et al. Chordoma Treatment with Boron Neutron Capture Therapy (BNCT): Experimental Insights. *Proceedings*, 2024, **95** (1), 13.

[17] Licitra L., Orlandi E., Bossi P., et al. Developing a trial design to establish BNCT as clinical application: insight for the national italian center for oncological hadrontherapy (CNAO). *Health Technol.*, 2024, **14** (5), P. 1037–1041.

[18] Zhizhin K.Yu., Zhdanov A.P., Kuznetsov N.T. Derivatives of closo-decaborate anion $[B_{10}H_{10}]^{2-}$ with exo-polyhedral substituents. *Russ. J. Inorg. Chem.*, 2010, **55** (14), P. 2089–2127.

[19] Williams D.B.G., Lawton M. Drying of Organic Solvents: Quantitative evaluation of the efficiency of several desiccants. *J. Org. Chem.*, 2010, **75**, P. 8351–8354.

[20] Zhdanov A.P., Bykov A.Yu., Kubasov A.S., et al. Hydrolysis of nitrilium derivatives of the closo-decaborate anion $[2\text{-}B_{10}H_9(N{\equiv}CR)]^-$. *Russ. J. Inorg. Chem.*, 2017, **62**, P. 468–475.

[21] Avdeeva V.V., Malinina E.A., Kuznetsov N.T. Boron cluster anions and their derivatives in complexation reactions. *Coord. Chem. Rev.*, 2022, **469**, 214636.
[22] Gobbo P., Biesinger M.C., Workentin M.S. Facile synthesis of gold nanoparticle (AuNP)–carbon nanotube (CNT) hybrids through an interfacial michael addition reaction. *Chem. Commun.*, 2013, **49**, 2831.
[23] Gobbo P., Novoa S., Biesinger M.C., Workentin M.S. Interfacial strain-promoted alkyne–azide cycloaddition (I-SPAAC) for the synthesis of nanomaterial hybrids. *Chem. Commun.*, 2013, **49**, 3982.
[24] Liu Y.-S., Ray K.G., Jørgensen M., et al. Nanoscale Mg–B via surfactant ball milling of MgB_2: morphology, composition, and improved hydrogen storage properties. *J. Phys. Chem. C*, 2020, **124**, P. 21761–21771.
[25] Saldin V.I., Ignat'eva L.N., Nikolenko Yu.M., et al. Thermal conversions of chitosanium dodecahydro-*closo*-dodecaborate. *Russ. J. Inorg. Chem.*, 2010, **55**, P. 1221–1227.

Submitted 10 December 2025; accepted 11 February 2026

Information about the authors:

Arina A. Ivanova – Faculty of Chemistry, Higher School of Economics, Moscow, 101000, Russia; Kurnakov Institute of General and Inorganic Chemistry of the Russian Academy of Sciences, Moscow, 119991, Russia; ORCID 0009-0008-2568-0483; ivanova.arina112233@gmail.com

Arina D. Filippova – Kurnakov Institute of General and Inorganic Chemistry of the Russian Academy of Sciences, Moscow, 119991, Russia; ORCID 0000-0002-2725-8891; arifilippova@yandex.ru

Maria A. Teplonogova – Kurnakov Institute of General and Inorganic Chemistry of the Russian Academy of Sciences, Moscow, 119991, Russia; ORCID 0000-0002-4820-8498; m.teplonogova@gmail.com

Alexey A. Sadovnikov – Topchiev Institute of Petrochemical Synthesis, Russian Academy of Sciences, 119991, Moscow, Russia; Kurnakov Institute of General and Inorganic Chemistry, Russian Academy of Sciences, Moscow 119991, Russia; ORCID 0000-0002-3574-0039; sadovnikov@ips.ac.ru

Nikita A. Selivanov – Kurnakov Institute of General and Inorganic Chemistry of the Russian Academy of Sciences, Moscow, 119991, Russia; ORCID 0000-0001-7426-5982; goovee@yandex.ru

Andrey P. Zhdanov – Kurnakov Institute of General and Inorganic Chemistry of the Russian Academy of Sciences, Moscow, 119991, Russia; ORCID 0000-0003-4083-386X; zhdanov@igic.ras.ru

Konstantin Yu. Zhizhin – Kurnakov Institute of General and Inorganic Chemistry of the Russian Academy of Sciences, Moscow, 119991, Russia; ORCID 0000-0002-4475-124X; zhizhin@igic.ras.ru

Nikolay T. Kuznetsov – Kurnakov Institute of General and Inorganic Chemistry of the Russian Academy of Sciences, Moscow, 119991, Russia; ORCID 0000-0002-0131-6387; boron@igic.ras.ru

Conflict of interest: the authors declare no conflict of interest.